Available online at www.sciencedirect.com
SCIENCE DIRECT®
International Journal of Heat and Fluid Flow 24 (2003) 645–656
International Journal of HEAT AND FLUID FLOW
www.elsevier.com/locate/ijhff

The kinematics of bend-induced mixing in micro-conduits

Mingqiang Yi, Haim H. Bau *

Department of Mechanical Engineering and Applied Mechanics, University of Pennsylvania, 297 Towne Building, 220 S. 33rd Street, Philadelphia, PA 19104-6315, USA

Received 19 March 2002; accepted 14 March 2003

Abstract

The absence of turbulence and the difficulty associated with introducing moving components into micro-fluidic systems make the mixing problem in micro-devices challenging. We studied steady, laminar, incompressible flow through a sequence of conduits with rectangular cross-sections aligned to form 90° with each other. The feasibility of taking advantage of bend-induced vortices to stir the fluid and enhance the mixing process was evaluated theoretically and experimentally. Since at very low Reynolds numbers the bend-induced vortices decay rapidly, it was necessary to utilize a large number of bends to achieve the desired effects. Since it is not practical to directly simulate the flow through a large number of bends, we borrowed Jones et al.'s [J. Fluid Mech. 209 (1989) 335–357] idea of constructing a two-dimensional map to project fluid particles from a cross-section upstream of the bend to a cross-section downstream of the bend. This map was then applied repetitively to trace particle trajectories in various bend arrangements. Under certain conditions, chaotic advection was predicted. A prototype of a stirrer was fabricated with low temperature co-fired ceramic tapes.

Keywords: Micro-fluidics; Chaotic advection; Mixing; Stirrer; Laboratory on a chip; Micro-total analysis

1. Introduction

In recent years, there has been a growing interest in developing minute laboratories on a "chip" and micro-chemical reactors (Jensen, 2001). Often, in order to facilitate chemical and biological reactions, one needs to mix various reagents and chemicals. Although the characteristic lengths associated with micro-devices are small, typically on the order of 100 μm, in the case of large molecules, diffusion alone does not provide sufficiently rapid means for mixing. For example, at room temperature, myosin's coefficient of diffusion in water is about 10^{-11} m^2/s, and the time constant for the diffusion along a length of 100 μm is intolerably large, about 10^3 s. Commonly, one encounters only low Reynolds number flows in micro-devices, and turbulence is not available to provide stirring. Moreover, it may not be feasible to incorporate moving components such as stirrers into micro-devices. Thus, one is forced to look for alternatives in order to make the mixing process more efficient.

Our work was motivated by flow visualization experiments that we carried out in our laboratory. Using ceramic tapes (Bau et al., 1998; Kim et al., 1998), we fabricated "Y–L" shaped conduits and capped them with glass slips. See Fig. 1. The conduits had square cross-sections with a 200 μm edge-length. We introduced, respectively, clear and dyed water into legs A and B of the "Y" driven by the same pressure head (Fig. 1). At Reynolds numbers of 10 or less, the dye and clear water remained well separated both upstream and downstream of the bend. At a Reynolds number of about 30, the dyed and clear water still remained separated in the straight segment upstream of the bend (Fig. 2). Once the flow passed the bend, however, the red dye spread to cover the entire conduit's width. This spreading was facilitated by the bend-induced counter-rotating vortices. Such vortices may assist the stirring process and enhance mixing.

Unfortunately, at low Reynolds numbers, the bend-induced vortices decayed before they had an opportunity to significantly stir the fluid. In order to increase the effect of these vortices, it was necessary to use a large number of bends. Since it was impractical to study the flow through a large number of bends using direct

* Corresponding author. Tel.: +1-215-898-8363; fax: +1-215-573-6334.
E-mail address: bau@seas.upenn.edu (H.H. Bau).

0142-727X/$ - see front matter © 2003 Elsevier Inc. All rights reserved.
doi:10.1016/S0142-727X(03)00026-2

Nomenclature

Re	Reynolds number
L_{DL}	flow development length
D_H	hydraulic diameter
D_{AB}	diffusion coefficient
Sc	Schmidt number
x, y	Cartesian coordinates within the conduit's cross-section
z	a coordinate along the channel's length
Ω	vortex strength
u, v, w	velocity components
$\dot{x}$, $\dot{y}$, $\dot{z}$	tracer particle velocity components
ϵ_L	relative pressure drop
ΔP_L	pressure drop in L-shaped channel
$\Delta P_\parallel$	pressure drop in straight channel
L	channel length
IL	relative interface length
$Z = x + iy$	points in the inlet (A) cross-section
$W = \xi + i\eta$	points in the exit (B) cross-section
S	mapping Z to W
R	rotational transformation
s	one-dimensional coordinate along the cross-section's edge
n	number of generations

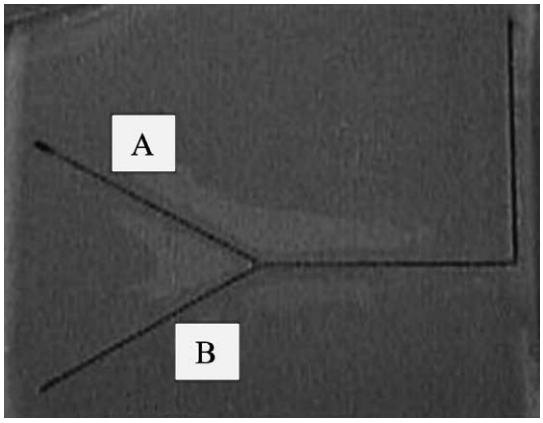

Fig. 1. A "Y–L" glass-capped conduit fabricated in low-temperature, co-fired ceramic tapes. The conduit cross-section is 200 μm × 200 μm. The conduit is capped with a glass cover to facilitate flow visualization.

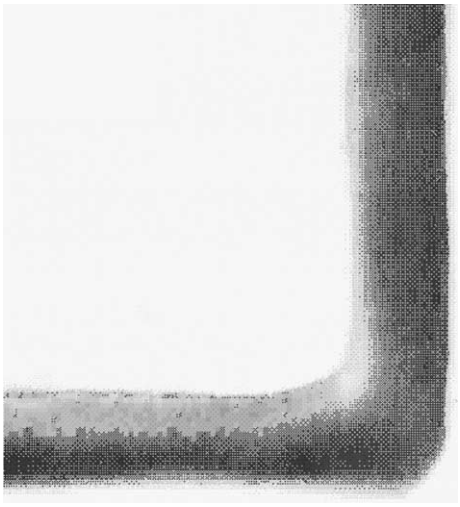

Fig. 2. A flow visualization experiment. $Re \sim 30$. Clear and dyed water were, respectively, injected into legs A and B of the "Y" (Fig. 1). Upstream of the bend, the dyed and clear liquids were well separated. Downstream of the bend, the dye spread to cover the entire width of the conduit.

numerical simulations, we followed ideas articulated in Jones et al. (1989) (to which for brevity's sake, we refer hereafter as JTA). JTA studied steady, laminar, incompressible flow through a twisted (coiled) pipe with a circular cross-section. Each pipe segment (basic cell) consisted of a semi-circle. Each cell was rotated (or twisted) with respect to the preceding one. JTA modeled the flow using Dean's perturbation solution and constructed a two-dimensional map to compute the advection of particles from a cross-section upstream of the unit cell to a cross-section downstream of the same cell. The position of the particles was tracked as they advected downstream and their location in the pipe's cross-section was marked after they passed each basic-cell to form Poincaré cross-sections. Further insights into the flow dynamics were obtained by constructing a one-dimensional map of the pipe's boundary onto itself. For sufficiently high Reynolds numbers, JTA demonstrated the presence of chaotic advection in twisted pipes. In the context of macro-scale systems, the ideas articulated in JTA have been put into practice for heat transfer (Acharya et al., 1992; Mokrani et al., 1997) and chemical reactions (Sawyers et al., 1996) enhancement.

Micro-fabrication technology is often planar in nature and the manufacturing of coiled tubes may not be feasible. As an alternative, one may fabricate bends connected with straight tube segments. Analogous to the case of the coiled tubes, the bends induce secondary circulation that enhances the stirring process. For example, Stremler et al. (2000) and Liu et al. (2000) micro-fabricated two- and three-dimensional "twisted" conduits in polydimethylsiloxane (PMDS) (Stremler et al., 2000) and in silicon (Liu et al., 2000). The "mixers" consisted of sequences of short, straight conduits having rectangular cross-sections. Each conduit formed a 90° angle with the preceding one. The conduits were arranged in various ways. In one configuration (case A), all the conduits lay in the same plane (a "square wave"

arrangement with a repeating unit cell consisting of four bends) (Stremler et al., 2000; Liu et al., 2000). This is analogous to JTA's twisted pipe with zero and 180° twist angles. In this arrangement, the symmetry of the flow is preserved. In another arrangement (Stremler et al., 2000) (case B, a serpentine conduit with a repeating unit cell consisting of six bends), no three adjacent conduits lay in the same plane. This is analogous to JTA's twisted pipe with 90° or 270° twist angles. Arrangement B destroys the symmetry of arrangement A and therefore makes for a more efficient stirrer. Arrangement B was found to be too complicated to implement in silicon (Liu et al., 2000). Instead, a third arrangement (C) was designed (Liu et al., 2000), consisting of twisted pairs of bends with each pair forming a "C"-shape. Arrangement "C" provides for better stirring than the planar configuration (A) but makes a poorer stirrer than arrangement B.

In this paper, we conducted a numerical study of the kinematics of the flow through a sequence of bends with the bends being arranged in various configurations. Instead of using periodic boundary conditions to investigate the flow in a "unit cell" of the stirrer, we simulated the flow field through a single bend and constructed a map that transformed particles from a cross-section upstream of the bend to a cross-section downstream of the bend. This method has the advantage that the above described map together with a "rotation" map allows one to simulate the kinematics of the flow through a variety of bend configurations. Here we analyze only arrangements A and B. In contrast to JTA, the numerical computations were not restricted to very low Reynolds numbers. Our approach, however, led to a discrete map (in a table format) that necessitated the use of interpolation in order to advance passive tracers when their initial positions were not explicitly tabulated. This interpolation scheme led to some loss of precision. We believe, however, that at least qualitatively we successfully captured the main features of the flow. The maps were then applied repetitively to simulate the process when the fluid passes through a large number of both planar and out of plane bends. We tracked the deformation and elongation of the interface between two different fluids. Like JTA, we also constructed a map of the conduit's boundary onto itself. Finally, both non-planar and planar configurations can be easily manufactured with ceramic tapes. We fabricated a stirrer of type B and crudely tested its performance. The fabrication procedure is described later in the paper. An abbreviated version of this paper appeared in Yi and Bau (2000).

2. Flow around a single bend

Consider short, straight flow conduits with square cross-sections. The basic cell consists of two straight

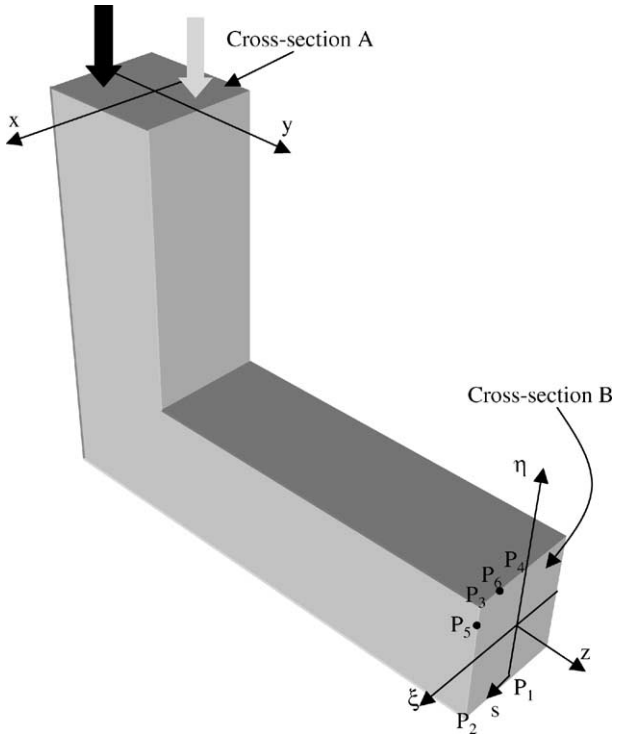

Fig. 3. The bend geometry and the coordinate system. Cross-sections A and B are, respectively, the inlet and exit cross-sections. Two immiscible fluids are introduced in cross-section A. Initially, one fluid occupies the region $y < 0$, and the other fluid occupies the region $y > 0$.

conduits connected at a 90°-angle. The "basic cell" and the coordinate systems are depicted in Fig. 3. The cross-section's edge length is the length scale. The x–y coordinates, $-1/2 \leqslant x \leqslant 1/2$ and $-1/2 \leqslant y \leqslant 1/2$, span the inlet's cross-section. The z-coordinate is aligned with the conduit's axis, and its origin is located at bend's center. Fully developed flow conditions are specified at both the inlet and the exit. The inlet and exit are located at distances $|z| > L_{DL} = 0.1 D_H Re$, where L_{DL} is the development length for laminar flow. The Navier–Stokes equations were solved with the commercial software package CFD2000 (2000). Computations were carried out with various mesh sizes to ensure that the results were reasonably mesh size-independent. Typically $30 \times 30 \times 160$ grid points were used, respectively, in the x, y, and z directions.

When $Re = 80$, Fig. 4a and b depict, respectively, the transverse velocity field at two cross-sections downstream of the bend and the streak lines as the flow passes through the bend. Upstream of the bend, the flow was unidirectional. As the flow approached the transverse bottom plane, the fluid was deflected (Fig. 4b) and formed two symmetric, counter-rotating, transverse vortices (Fig. 4a). These vortices advected downstream with their intensity diminishing rapidly and their center of rotation migrating upwards. This vortex pair existed even when the Reynolds number was very small. We defined the vortex strength,

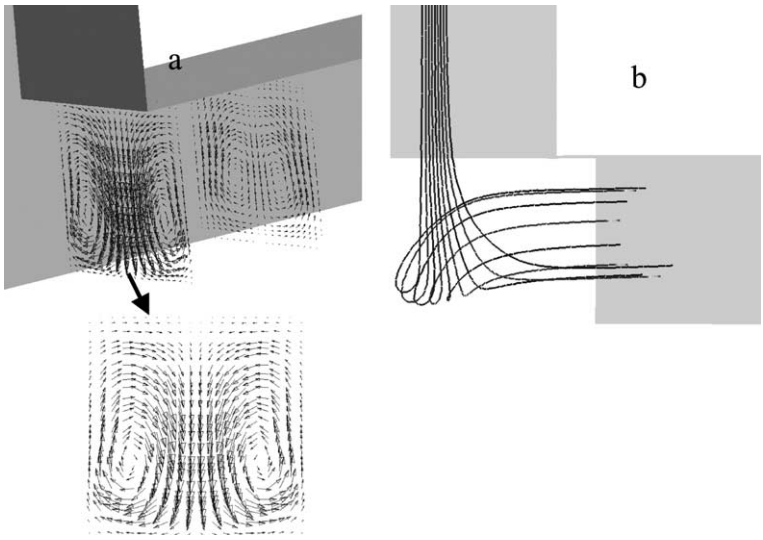

Fig. 4. (a) The velocity vector field is depicted at various cross-sections downstream of the bend. (b) Fluid trajectories are depicted as the flow goes around the bend. $Re = 80$.

$$\Omega(Re,z) = \int_{A_{\text{cross-section}}} \left(\frac{\partial u}{\partial y} - \frac{\partial v}{\partial x}\right)^2 \mathrm{d}x\,\mathrm{d}y, \tag{1}$$

where u and v are, respectively, the velocity components in the x and y directions. Fig. 5 depicts on a semi-log scale the ratio $\Omega(Re,z)/\Omega(Re,0.5)$ as a function of (z) when $Re = 1$, 5, 10, 20, 40, and 80. $z = 0.5$ is the entry cross-section to the conduit's segment downstream of the bend. Witness the nearly exponential decay of the vortex. Using least squares, the data in Fig. 5 was fitted with

$$\Omega(Re,z) = \Omega\left(Re,\frac{1}{2}\right)\exp\left(-f(Re)\left(z-\frac{1}{2}\right)\right). \tag{2}$$

Both $\Omega(Re,0.5)$ and $f(Re)$ are depicted as functions of the Reynolds number in Fig. 6. The symbols and solid lines correspond, respectively, to best-fit curves and to computational results

$$f(Re) \sim 7.5Re^{-0.27},$$

$$\Omega(Re,0.5) = \begin{cases} 7\times10^{-3}Re^2 + 0.058Re + 0.84 \\ \quad (0 < Re < 10), \\ 0.18Re + 0.41 \\ \quad (10 < Re < 80). \end{cases}$$

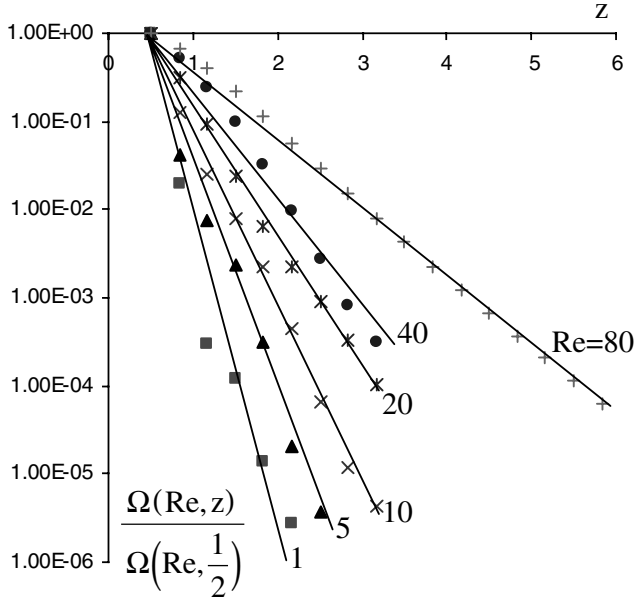

Fig. 5. The relative vortex intensity (symbols), $\Omega(Re,z)/\Omega(Re,0.5)$, is depicted as a function of (z) when $Re = 1$, 5, 10, 20, 40, and 80. The solid lines are best-fit curves.

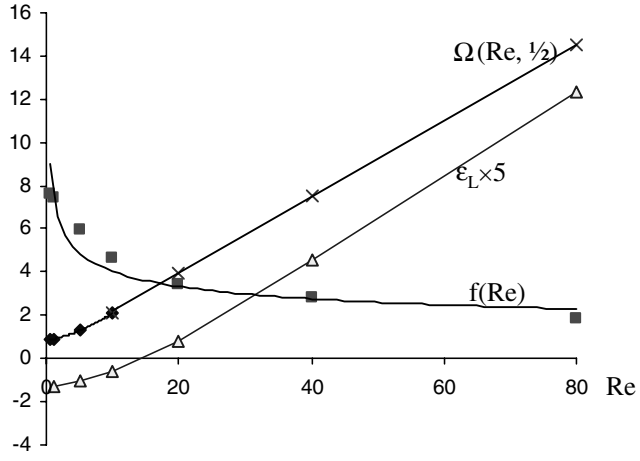

Fig. 6. The vortex intensity $\Omega(Re,0.5)$, the vortex decay rate $f(Re)$, and the relative pressure penalty $\varepsilon_L = (\Delta p_L - \Delta p_\parallel)/[(D_H/L)\Delta p_\parallel]$ for flow around a "L-shaped" bend are depicted as functions of the Reynolds number. In the above, ΔP_L and $\Delta P_\parallel$ correspond, respectively, to the pressure drop around a bend and in a straight conduit. The solid lines are best-fit curves.

Since we are considering very low Reynolds numbers, viscous effects dominated and the vortices decayed rapidly. For example, when $Re = 80$, the vortex strength decayed 1000-fold within six hydraulic diameters from the corner. Thus, for the range of Reynolds number considered in this work, it was reasonable to assume fully developed conditions about 10 hydraulic diameters downstream from the corner.

At very low Reynolds numbers, the presence of the bend did not contribute significantly to pressure losses. Fig. 6 also depicts the relative pressure drop $\varepsilon_L = (\Delta P_L - \Delta P_{\|})/(P_{\|} * D_H/L)$ for flow through a L-shaped bend as a function of the Reynolds number. To improve visibility, the relative pressure drop was multiplied by a factor of 5. ΔP_L and $\Delta P_{\|}$ denote, respectively, the pressure drop in the L-shaped bend and in a straight conduit of equivalent length. The straight conduit's length was measured along the L-shaped conduit's axis. At very low Reynolds numbers, the pressure drop in the L-shaped conduit was actually smaller than in the straight conduit. This can be attributed to the bend providing a larger cross-sectional area for the flow than the straight conduit does. When $Re > \sim 15$, the secondary flow started to take its toll and the pressure loss in the L-shaped conduit increased above the corresponding value for the straight conduit. The pressure "penalty" was correlated (solid line in Fig. 6) as

$$\varepsilon_L = \frac{\Delta p_L - \Delta p_{\|}}{(D_H/L)\Delta p_{\|}} \sim 1.27 \times 10^{-4} Re^2 + 0.025 Re - 0.334. \quad (3)$$

The two vortices that formed at the bend deform material lines. To illustrate this effect, consider two immiscible fluids entering the bend through cross-section (A) and being initially separated by the interface $y = 0$ (Figs. 3 and 7a). The two fluids are identical except for their "color". As the two fluids emerge through the exit cross–section B, the interface between them stretches, deforms, and folds. Fig. 7b–d depict, respectively, the areas occupied by the two fluids in cross-section B when $Re = 10$, 40, and 80. As the interfacial length increases, the two materials are brought into closer contact, making inter-diffusion more effective. The same mechanism is likely to enhance transport of mass and heat between the fluid and the conduit's walls. Fig. 8 depicts the relative length of the interface (IL) as a function of the Reynolds number when the fluids emerge from cross-section B. The length of the interface (IL) is nearly a linear function of the Reynolds number, IL $\sim 1 + 0.04Re$, when $0 < Re < 80$.

Figs. 7 and 8 illustrate that the corner-induced vortices provided a means for fluid stirring and explain the experimental observation (Fig. 2) of the blending of the

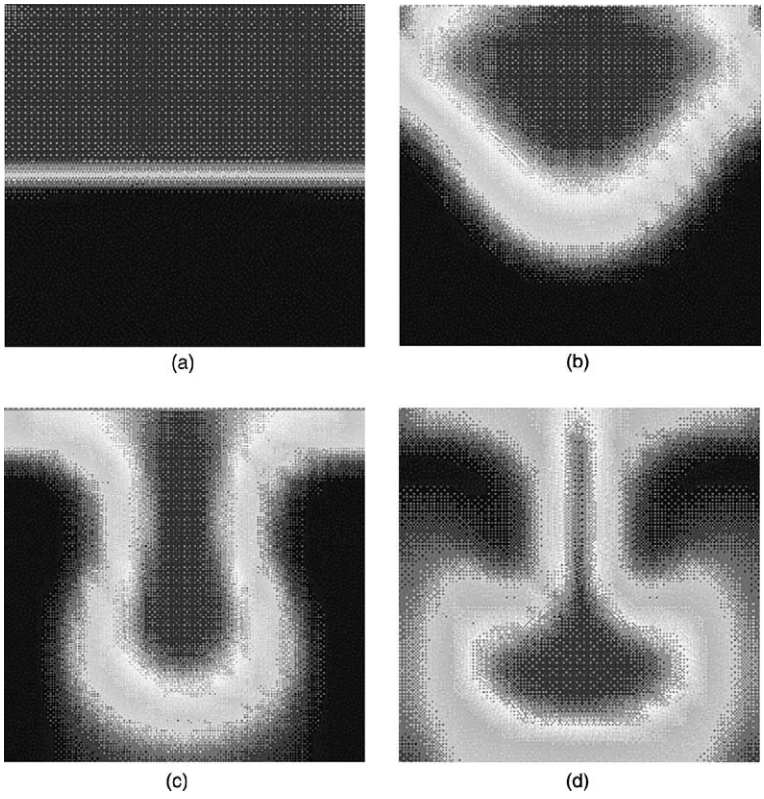

Fig. 7. Two fluids separated by the interfacial line $y = 0$ enter through inlet A (a). The cross-sectional areas occupied by the two fluids as they emerge through cross-section B downstream of the bend are shown when $Re = 10$ (b), $Re = 40$ (c), and $Re = 80$ (d).

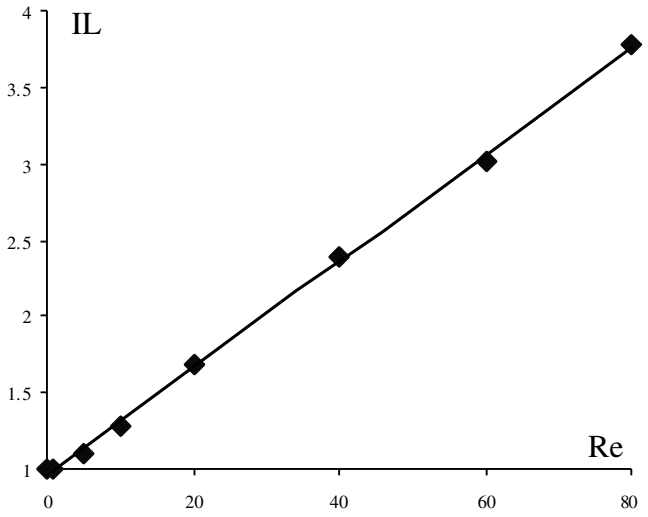

Fig. 8. The length of the interface (IL) in the exit cross-section, B, is depicted as a function of the Reynolds number for flow around a single bend. The solid line is a best-fit line.

dyed and clear fluids downstream of the bend. This mixing enhancement increased as the Reynolds number increased. Unfortunately, flows in micro-channels are typically at very low Reynolds numbers and the stirring induced by a single bend may not be sufficient to ensure efficient mixing. A fairly large number of bends are likely to be required to achieve desired effects. It would not be practical, however, to study the flow through a large number of bends using direct numerical simulations. One would typically use periodic boundary conditions to simulate the process that takes place in a single cell. Instead, following JTA, we constructed the map, $W = S(Z)$, that transforms points from the entry cross-section (A) to the exit cross-section (B). In the above, $Z = x + \mathrm{i}y$ and $W = \xi + \mathrm{i}\eta$ refer, respectively, to points in the inlet (A) and exit (B) cross-sections. Once the map S is available, it can be manipulated in conjunction with a rotational map (see below) to study the flow field through various bend configurations.

3. Mapping of points from the entry to the exit cross-sections

In this section, we describe the construction of the map, S, that transforms points from the inlet to the exit cross-sections. In contrast to JTA, a simple analytic expression capable of describing our flow field is not available, and we were forced to resort to numerical techniques in order to construct the map, S.

The trajectories of individual fluid particles were obtained by integrating the equations:

$$\dot{x} = u(x,y,z); \quad \dot{y} = v(x,y,z); \quad \text{and} \quad \dot{z} = w(x,y,z). \tag{4}$$

In the above, u, v, and w are, respectively, the velocity components in the x, y, and z directions, and the dot represents a time-derivative. We divided the entrance cross-section (A) into a square grid consisting of 21×21 grid points. Then, we followed the trajectories of particles starting at each of the grid points, i.e., at $Z = x + \mathrm{i}y$, and tabulated the corresponding location at which the trajectories penetrated the exit cross-section B: $W = S(Z) = \xi(x,y) + \mathrm{i}\eta(x,y)$. Note that time is excluded from the map. Trajectories starting simultaneously at different points in (A) penetrated cross-section (B) at different times. The map is symmetric with respect to the y-axis, i.e., $S(-x + \mathrm{i}y) = -\xi(x,y) + \mathrm{i}\eta(x,y)$.

Since the map, S, was discrete, we were forced to construct an interpolation scheme to map points that were not explicitly tabulated. Each of the square grid elements in the entrance cross-section (A) was endowed with local coordinates with the corner points being denoted as $\{0,0\}$, $\{1,0\}$, $\{0,1\}$, and $\{1,1\}$. The corresponding mapping of these points in the exit plane (B) was explicitly available in the table and was denoted as $\{\xi(0,0), \eta(0,0)\}$, $\{\xi(0,1), \eta(0,1)\}$, $\{\xi(1,0), \eta(1,0)\}$, and $\{\xi(1,1), \eta(1,1)\}$. The mapping of any point $\{x,y\}$ within the square was computed by an interpolating formula similar to what is being used in finite element algorithms:

$$\begin{aligned}\xi(x,y) &= (1-x)(1-y)\xi(0,0) + (1-x)y\xi(0,1) \\ &\quad + x(1-y)\xi(1,0) + xy\xi(1,1), \\ \eta(x,y) &= (1-x)(1-y)\eta(0,0) + (1-x)y\eta(0,1) \\ &\quad + x(1-y)\eta(1,0) + xy\eta(1,1).\end{aligned} \tag{5}$$

The interpolation scheme assumed that small area elements deformed in such a way that straight lines connecting two nearby grid points in cross-section (A) remained nearly straight under the transformation. This is not strictly correct. One can eliminate this shortcoming through the use of non-linear (higher order) interpolation schemes. At low Reynolds numbers, the error resulting from this quasi-linear approximation (5) appeared, however, to be tolerable. We validated the mapping by comparing results that were obtained by repetitive use of the map with results of direct numerical simulations. For example, when $Re = 10$, Fig. 9 depicts the predicted deformation of the line $y = 0$ as the flow goes around 2 and 3 bends. The line was mapped using both direct numerical simulation (squares) and repetitive use of the map $S(Z)$ (triangles). The results obtained from these two techniques were in reasonable agreement.

Not surprisingly, the map $S(Z)$ did not preserve area. Since fluid particles in the vicinity of the cross-section's center experience higher axial velocity than particles close to the conduit's walls, mass conservation dictated that the area of a material's blob should shrink as the material migrated towards the cross-section's center. The quantity that was preserved under the map was the

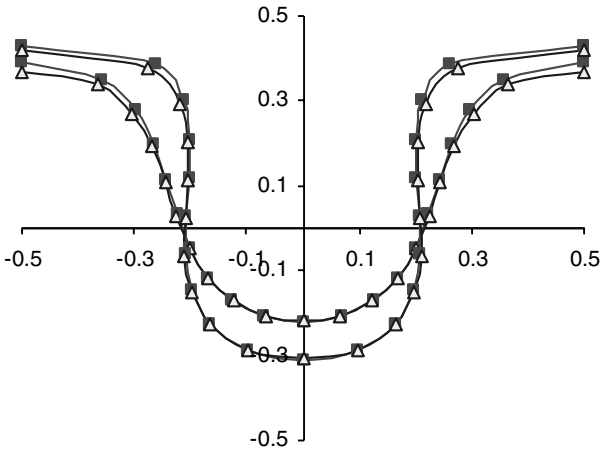

Fig. 9. The deformation of the line $y = 0$ when $Re = 10$ as the flow passes 2 and 3 bends is shown. The results of the direct numerical simulations are depicted by squares. The results obtained using the mappings $W = S^2(Z)$ and $W = S^3(Z)$ are depicted using upright triangles.

volumetric flow rate, $\int_{\Delta A} u(x,y)\,\mathrm{d}x\,\mathrm{d}y$. For example, in a few calculations (not shown here), we demonstrated that

$$\frac{S^n\left(\int_{\Delta A} u(x,y)\,\mathrm{d}x\,\mathrm{d}y\right)}{\int_{\Delta A} u(x,y)\,\mathrm{d}x\,\mathrm{d}y} \sim 1,$$

when plotting the above ratio as a function of (n) for various small area elements (ΔA).

Finally, following JTA, we constructed a map of the boundary onto itself. Owing to the non-slip boundary condition, fluid particles attached to the conduit's walls did not move in finite time. Time was, however, eliminated from the map, S. The mapping of the boundary can be viewed as an asymptotic limit when time goes to infinity. To make the idea more concrete, consider, for example, the conduit's wall located at $x = 0.5$. We denoted the local coordinate normal to the wall as $\zeta = 0.5 - x$. Accordingly, the wall was located at $\zeta = 0$. Next, we expanded the three velocity components into Taylor series in terms of ζ, about $\zeta = 0$. The expansion revealed that the normal velocity to the wall $u \sim \zeta^2$, while the tangential velocity components (v) and (w) in the y and z directions were (generally) proportional to ζ. This is true because of the presence of the secondary, transverse flow. With the exception of a few isolated points, the vorticity was not zero next to the wall. Therefore, Eq. (2) suggest that as $\zeta \to 0$, $\mathrm{d}x/\mathrm{d}z = 0$ and $\mathrm{d}y/\mathrm{d}z \neq 0$. In the context of the mapping S, points on the wall stay on the wall; but they are free to slip along the wall. Similar arguments hold for the symmetry line. Thus, one can construct a one-dimensional map, T, mapping points on the boundary of the inlet cross-section A to points on the boundary of the exit cross-section B. We obtained the one-dimensional map, T, by integrating Eq. (2) and tracking the trajectories starting with an initial point, Z, at the wall's vicinity in cross-section A; obtaining the corresponding point $W = S(Z)$ in cross-section B; gradually reducing the normal distance from the wall (ζ); and finally extrapolating to $\zeta \to 0$. We do not show the map here (for additional details, we refer the interested reader to Yi (2001)). The map revealed the presence of a number of fixed points. To identify the location of the various points, we used the "wall" coordinate (s). The intersection of the symmetry line with the bottom boundary (point P_1 in Fig. 3) is located at $s = 0$ and $s = 3$. $s = 0.5$ and 1.5 correspond, respectively, to the lower (P_2) and upper (P_3) corners. $s = 2$ corresponds to the intersection of the symmetry line with the upper boundary (Point P_4 in Fig. 3). The segment $2 < s < 3$ corresponds to the symmetry line. Points P_1 and P_4 are saddle points with the symmetry line forming an hetroclinic connection and serving as an unstable manifold for P_4 and the stable manifold for P_1. The map T reveals the presence of two additional fixed points, P_5 and P_6. The approximate location of these points is sketched in Fig. 3. The sink, P_5, was located on the side-wall at $0.5 < s_5 < 1.5$. The source, P_6, was located on the top-wall at $1.5 < s_6 < 2$. The presence of these two fixed points suggests the existence of a corner eddy with the hetroclinic connection between P_5 and P_6 serving as a separatrix between the main vortex and the corner vortex. Surprisingly and perhaps due to lack of precision, we were not able to observe this vortex in our numerical simulations. As the Reynolds number increased, P_5 and P_6 migrated towards each other until, at $Re \sim 40$, both fixed points collapsed to form a single saddle point at the corner $s = 1.5$. JTA also observed the presence of fixed points in their one-dimensional map of the boundary.

The availability of the one- (T) and two- (S) dimensional maps together with the rotational map $R = \exp(\mathrm{i}m\pi/2)$, where m is an integer, allows us to study the flow as it goes through a large number of bends with the bends being arranged in different ways. For example, Fig. 10 depicts a number of possible arrangements and the corresponding mappings. In most of these studies, we followed the evolution of the interface $y = 0$. This interface can be envisioned as if it were separating two different fluids entering through cross-section A (Fig. 1).

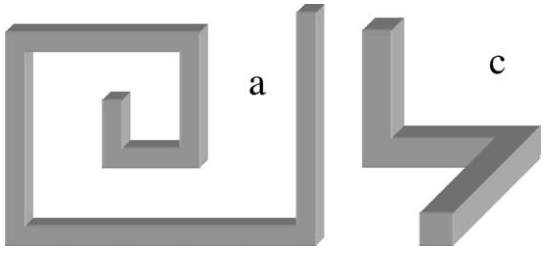

Fig. 10. A sample of various arrangements of conduits and the corresponding transformations that can be used to map particles from the inlet to the exit cross-section.

Furthermore, we focused only on kinematic effects (stirring) and ignored diffusion.

4. Planar configuration

Consider the planar structure depicted in Fig. 10a. A large number of bends were placed in series. The straight segments between the bends were sufficiently long to assure that the secondary flows died out and the flow became fully developed before it entered the subsequent bend.

We first traced the intersection points of the trajectories with the conduit's cross-section after each unit cell (Poincaré maps). When $Re = 10$, Fig. 11 depicts the intersections of four trajectories with initial positions at (± 0.4, 0) and (± 0.3, 0). Witness the presence of the closed (periodic) orbits. The periodic orbits were preserved for all the Reynolds numbers ($0 \leqslant Re \leqslant 80$) that we considered in this paper.

In order to illustrate the stirring effect of the bend-induced vortices, we considered two fluids (light and dark) that were separated by the line $y = 0$ when entering cross-section A. We then applied repetitively the mapping S. When $Re = 10$, Fig. 12 depicts the structure of the interface after the flow has passed through 1, 3, 5, 7, 20, and 40 bends. Through the action of the counter-rotating vortices, the interface between the two fluids elongated, deformed, and folded. The relative length of the interfacial line as a function of (n) is depicted in Fig. 13. The length of the interface (IL) increased nearly linearly with the number of bends and with the Reynolds number,

$$\mathrm{IL} \sim 1 + 0.04Re * n. \tag{6}$$

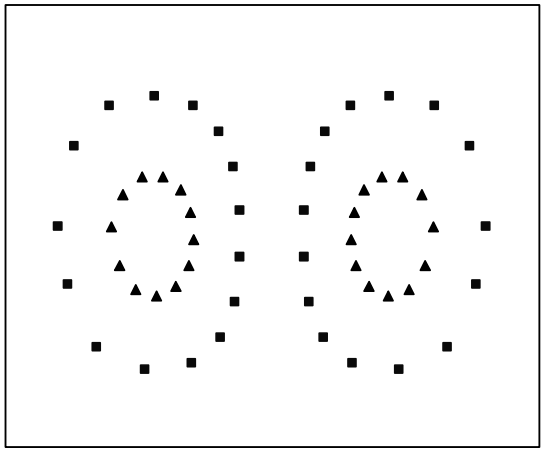

Fig. 11. A Poincaré map of the penetrations of two particle's trajectories through subsequent cross-sections downstream of the bend. The mixer's geometry is depicted in Fig. 10a. $Re = 10$.

In order to achieve the same elongation of the interface, one can either increase the number of bends or increase the Reynolds number in the same proportion. At low Reynolds numbers, the deformation induced by a bend could be nearly undone by aligning the subsequent bend in the opposite direction, i.e., $S(S(Ze^{i\pi})e^{i\pi}) \approx Z$. In other words, $S^{-1} \approx e^{i\pi}S(Ze^{i\pi})$.

When the bends were arranged in the plane, the symmetry with respect to the $x = 0$ axis was preserved.

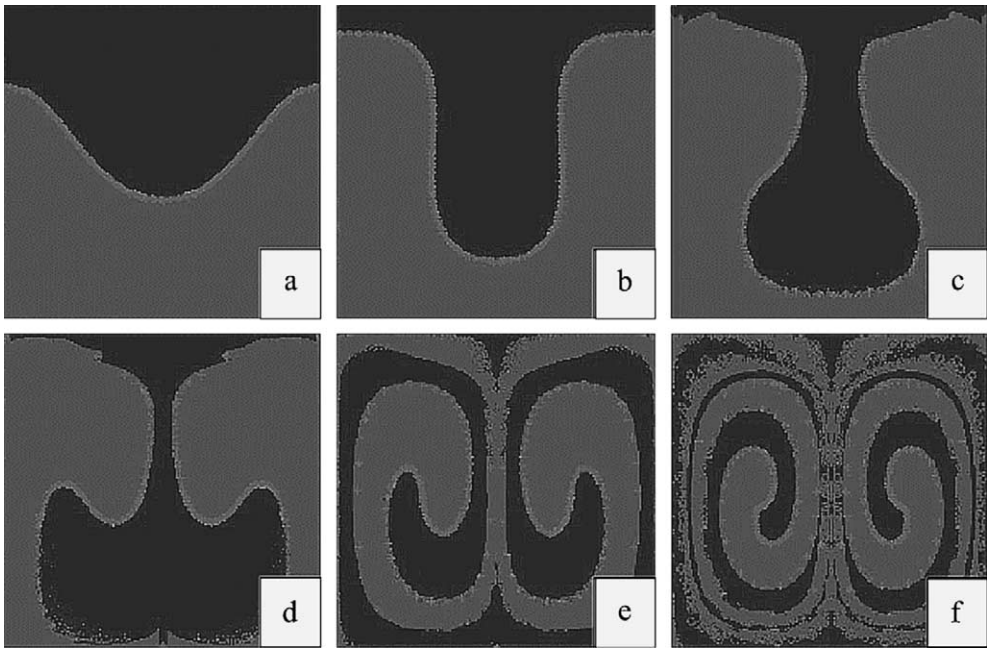

Fig. 12. The structure of the interface as the flow passes through n bends (a) $n = 1$; (b) $n = 3$; (c) $n = 5$; (d) $n = 7$; (e) $n = 20$; and (f) $n = 40$, $Re = 10$.

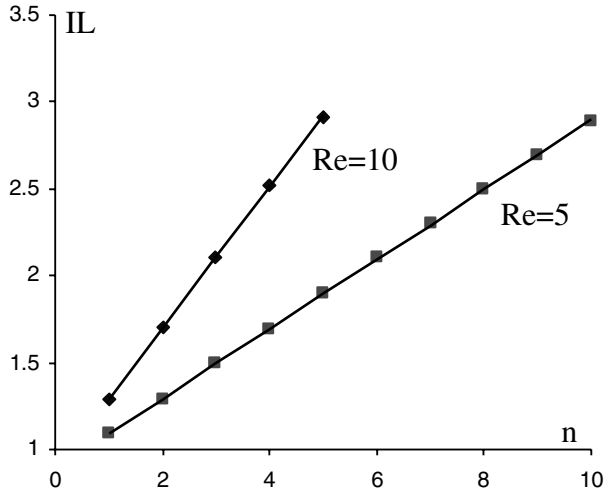

Fig. 13. The relative length of the interface is depicted as a function of the number of bends (n) when $Re = 5$ and 10. The solid line is a best-fit curve.

Fluid elements that started on one side of the symmetry line remained on the same side of the symmetry line indefinitely. In order to achieve a more efficient stirring, it was desirable to break this symmetry. This can be accomplished by introducing "out-of-plane" bends (i.e., Fig. 10c).

5. Three-dimensional configurations

Fig. 10c depicts a sequence of two bends with the three conduit segments being perpendicular to each other. The presence of the "out-of-plane" conduit destroyed the symmetry that existed when all the conduits were aligned in the same plane. To model the flow through the sequence of these two bends, we combined the map S with the rotation map $R = \exp(i\pi/2)$ that rotates a cross-section by 90°. For the geometry depicted in Fig. 10c, the map $S_2 = R^{-1}SRS$ describes the transformation from the inlet cross-section to the exit cross-section. When $Re = 10$, Fig. 14a and b describe the deformation of the interfacial line between two fluids that initially entered the device with a flat interface ($y = 0$). Fig. 14a depicts the results of a single application of the map S_2. Fig. 14b depicts the shape of the interface after the map S_2 was applied 5 times (i.e., S_2^5). Witness that the presence of the "out-of-plane bend" eliminated the symmetry that was inherent in the planar case.

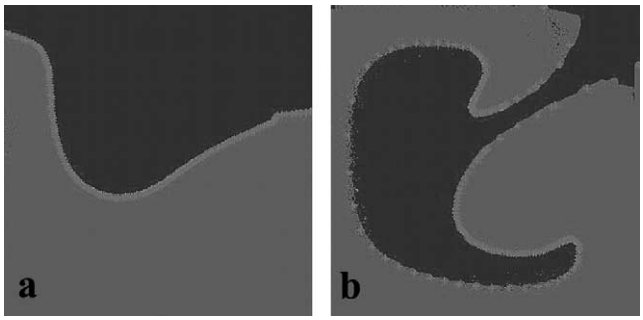

Fig. 14. The shape of the interface as the fluid goes through a sequence of three conduit segments (a) $n = 1$ and (b) $n = 5$. $Re = 10$. The conduit geometry is depicted in Fig. 10c.

The basic cell depicted in Fig. 10c can be extended in different ways. Fig. 15 depicts one example of such a three-dimensional configuration. The unit cell of this configuration is modeled by the application of the map $S_6 = RSR^{-1}SRSR^{-1}SR^{-1}SRS$.

When $Re = 10$, 20, and 40, Fig. 16a–c depict the results of repetitive application of the mapping S_6. In Fig. 16a ($Re = 10$), we depict the penetration points of trajectories starting at $Z = (-0.2, 0)$, (± 0.3, 0), and (0.3, 0.1). The trajectories seem to approximate periodic orbits with a periodicity of about 20. In other words, after 20 applications of the map S_6, the penetration points start to nearly repeat tracing what appears to be a chaotic cloud centered around a periodic orbit.

In Fig. 16b ($Re = 20$), we depict the penetration points of trajectories starting at $Z = (\pm 0.3, -0.1)$. The cross-section seems to be divided into two parts. The trajectories in one part of the cross-section appear to form a chaotic cloud about a periodic orbit with a periodicity of 10. The trajectories in the other part of the cross-section appear to be chaotic. In Fig. 16c ($Re = 40$), we depict the subsequent penetration points of trajectories starting at $Z = (0.3, -0.1)$. The figure represents 10^4 applications of the map S_6. The trajectories appear to be very irregular or chaotic. The chaotic behavior is present throughout most of the cross-section, and each fluid particle appears to visit almost every part of the cross-section. Such behavior is likely to lead to effective stirring.

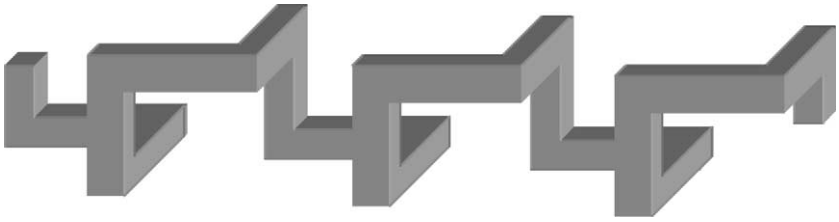

Fig. 15. The unit cell depicted in Fig. 10c is repeated numerous times to produce a three-dimensional stirrer.

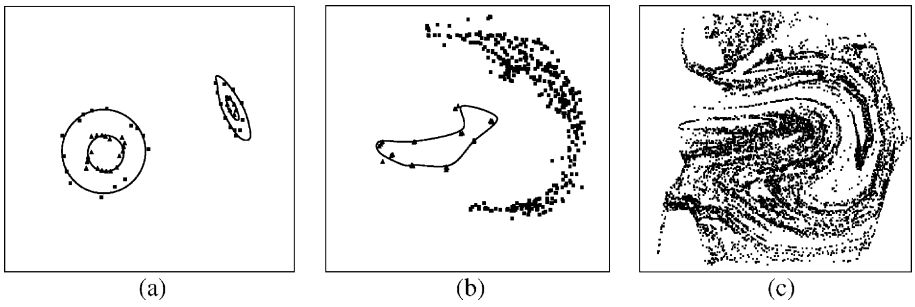

Fig. 16. The intersection points of the trajectory with the conduit's cross-section after each unit cell (S6). (a) $Re = 10$, starting points: (−0.2, 0), (±0.3, 0), and (0.3, 0.1); (b) $Re = 20$; starting point: (±0.3, −0.1); and (c) $Re = 30$; starting point: (0.3, −0.1). In Fig. (a) and (b), the penetration points were connected with lines for better visibility.

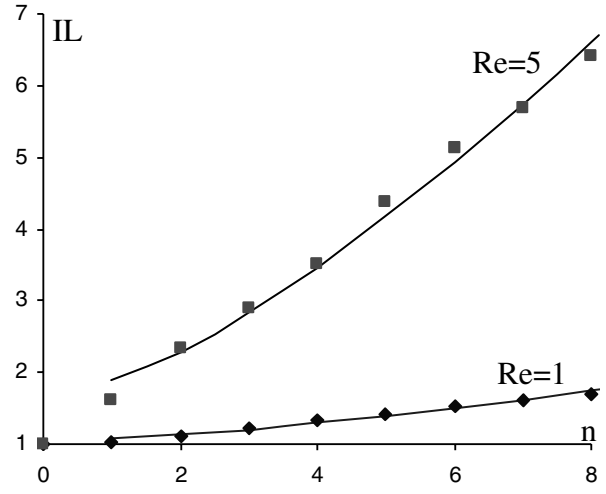

Fig. 17. The relative length of the interfacial as a function of the number of units (a). The solid lines are best-fit curves ($IL = f_1(Re) * n * \ln(n) + f_2(Re)$).

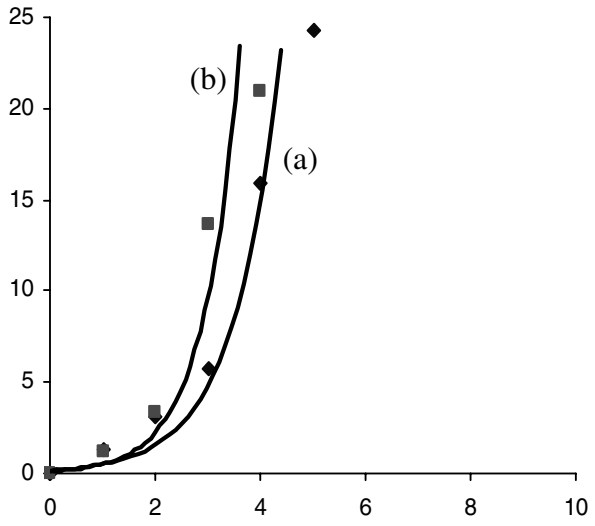

Fig. 18. The solid lines were fitting curves ($IL = IL_0 e^{\lambda n}$). (a) the initial line segment (0.35, 0)–(0.4, 0). (b) The initial line segment (−0.45, 0)–(−0.4, 0).

The appearance of chaotic behavior is hardly surprising. We denote the secondary flows induced by two subsequent bends as $B1$ and $B2$. A passive tracer particle will alternately be trapped in flow fields $B1$ and $B2$. When the two flow fields are rotated, the passive tracer will follow a zigzag path common to chaotic advection. This is very similar to the case when two different flow fields are alternated periodically in time. It is well known that the latter leads to (Aref, 1984; Yi et al., 2002; Qian and Bau, 2002; Qian et al., 2002) Lagrangian chaos.

We also examined the elongation of the interfacial line $y = 0$ under the mapping S^6. When $Re = 1$ and 5, Fig. 17 depicts the relative length of the interfacial line as a function of the number of units, n. The symbols in the figure represent the measured line length, and the solid lines are best-fit curves. It appears that the line elongated slightly faster than linearly and that the line length correlated well with $IL \sim f_1(Re) * n * \ln(n) + f_2(Re)$, where $f_1(1) \sim 0.04$, $f_1(5) \sim 0.28$, $f_2(1) \sim 1.07$, and $f_2(5) \sim 1.9$.

When the Reynolds number was further increased (i.e., $Re \geqslant 20$), we were no longer able to track the entire length of the interfacial line because of the very rapid stretching and folding. Instead, we selected individual segments, i.e., (a) $0.35 < x < 0.4$ and (b) $-0.45 < x < -0.4$. When $Re = 40$, Fig. 18 depicts the length of these line segments as functions of (n). The length grew like $e^{\lambda n}$, where $\lambda > 0$. For example, $\lambda \sim 1.12$ (a) and 1.45 (b). The magnitude of λ depended on the initial conditions, i.e., different line segments were elongated at different rates. λ can be interpreted as the Lyapunov exponent, and its being positive is indicative of chaotic advection.

Finally, we examined the mapping of the conduit's boundary (not shown here). When $Re \leqslant 10$, there were four fixed points on the boundary. When $Re > 20$, we observed only two fixed points on the boundary. We speculate that the other two fixed points migrated into

the cross-section's interior. The fact that two fixed points remained anchored on the boundary is probably responsible for the complicated hetroclinic tangle and the presence of large-scale chaos. For example, in numerical experiments, Aref et al. (1989) observed that when all the fixed points migrated from the boundary into the cross-section's interior, the chaotic behavior was confined to a small segment of the cross-section.

6. Device fabrication and testing

To illustrate that the ideas articulated here can, indeed, be put into practice, we fabricated a passive stirrer with low temperature, co-fired ceramic tapes (LTCC). Although the stirrer can be fabricated with various substrate materials ranging from silicon to polymers, we chose to construct our prototype with LTCCs because they facilitate easy, inexpensive, layered manufacturing, and a rapid prototyping platform.

In their pre-fired (green) state, the ceramic tapes consist of oxide particles, glass frit, and organic binder (that can be made from photoresist). The tapes are typically cast with a thickness starting at 40 μm. Pre-fired tapes can be machined by laser, milling, chemical means, and photolithography (when the binder is photoresist). Metallic paths can be either screen-printed or processed photolithographically to form electrodes, resistors, conductors, and thermistors. Conduit sizes may range from ~10 μm to a few millimeters. Upon firing, the organic binder burns out, the oxide-particles sinter, and the tapes solidify. Many tapes (>80) can be stacked together, aligned, laminated, and co-fired to form monolithic structures with complex, three-dimensional mazes of fluidic conduits, electronic circuits, and electrodes. Glass windows and other materials can be readily attached to the tapes to facilitate optical paths. Multiple layers of coils can be embedded in the tapes to generate magnetic fields. For additional details, see Bau et al. (1998).

Fig. 19 depicts an exploded view of a stirrer design. The device consisted of five layers which in their pre-fired state were about 225 μm thick. Rectangles of the desired size were blanked from the raw material. 90 degree bends were milled in layers 2 and 4. Layer 3 provided interconnects (vias) between these two layers. The vias, together with the conduit segments in layers (2) and (3), formed "out-of-plane" bends. The individual layers were than stacked, aligned, laminated, and co-fired to form a monolithic block with the conduit geometry depicted in Fig. 15.

To facilitate flow visualization, we fabricated a slightly different device than the one depicted in Fig. 19. More specifically, we replaced layers 1 and 5 with glass slides. In order to bond the glass, layers 2–4 were co-fired. Subsequently, the glass (with a matching thermal expansion coefficient) and the fired tapes were stacked and heated above the glass transition temperature. The glass formed a hermetic bond with the ceramics. A top view photograph of an actual device with a glass cover is shown in Fig. 20.

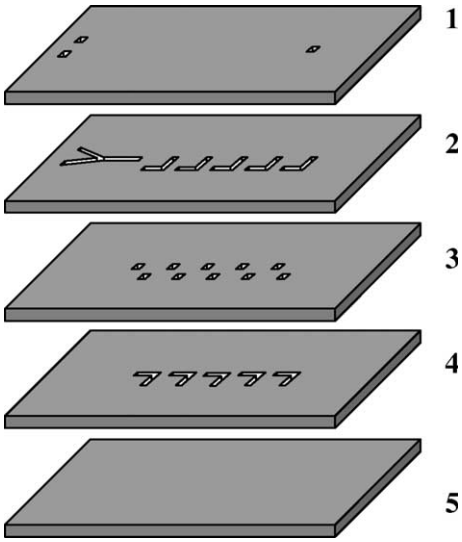

Fig. 19. An exploded view describing the fabrication of the passive mixer. Layers 2 and 4 contain 90° bends. Layer 3 provides vertical interconnects between layers 2 and 4. These vertical interconnects, together with the planar conduits, form the out of plane bends. Layer 1 contains the inlet and exit ports.

Using identical pressure heads, we introduced clear and dyed water into the two legs of the V on the left-hand side of Fig. 20. As the two legs merged into a single straight section, the dye and the clear water remained well separated even when the Reynolds number

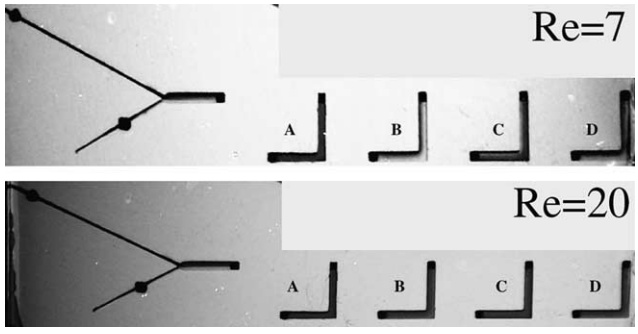

Fig. 20. Photographs of an actual device fabricated with ceramic tapes. To facilitate flow visualization, layers 1 and 5 (in contrast to Fig. 19) were made out of glass slides. Clear and dyed water were introduced through the V-section. When $Re = 7$, the dye and clear water remain well separated even after going through a few generations of bends. In generations A and C, the dyed water is on top of the clear water. In generations B and D, the dye and clear water are side by side. When $Re = 20$, the clear and dyed water remain well separated in the inlet section but appear to be well mixed downstream. No separation is evident between the clear and dyed water in generations A–D.

exceeded 40. When $Re = 7$, the dye and clear water also remained well separated after going through a few generations of bends. In generations A and C (Fig. 19a), the dye is on top of the clear water. In generations B and D, the dye and clear water are side by side. When $Re = 20$, the clear and dyed water appear to be well mixed downstream of the first bend and no separation is evident between them. Unfortunately, due to the very small size of the conduits, we were not able to carry out detailed experiments to delineate the morphology of the interface between the two fluids.

7. Conclusion and discussion

Secondary flows induced by bends can stir fluids, enhance mixing, and under certain conditions induce chaotic advection. A sufficient length was allowed downstream of each bend to allow the establishment of fully developed flow conditions. Shorter lengths than the ones considered here are likely to induce an even more intense stirring process. To be effective, this type of stirrer needs to be operated at Reynolds numbers exceeding 10. The stirrer can be easily fabricated using various layered manufacturing techniques such as ceramic tapes. Interestingly, the stirrer does not significantly increase the pressure drop.

The sequence of bends that we described in this paper is also useful to enhance the transport between the wall and the bulk of the fluid and thus may also be used to enhance heat transfer and mass exchange between the bulk of the fluid and the solid wall.

Acknowledgements

The work described in this paper was supported, in part, by DARPA through grant N66001-97-1-8911 to the University of Pennsylvania.

References

Acharya, N., Sen, M., Chang, H.C., 1992. Heat transfer enhancement in coiled tubes by chaotic mixing. Int. J. Heat Mass Transfer 35, 2475–2489.

Aref, H., 1984. Stirring by chaotic advection. J. Fluid Mech. 143, 1–21.

Aref, H., Jones, S.W., Mofina, S., Zawadzki, I., 1989. Vortices, kinematics and chaos. Physica D 37, 423–440.

Bau, H.H., Ananthasuresh, G.K., Santiago-Aviles, J., Zhong, J., Kim, M., Yi, M., Espinoza-Vallejos, P., 1998. Ceramic tape-based systems technology. Micro-Electro-Mechanical Systems (MEMS), DSC vol. 66. pp. 491–498.

CFD2000, Adaptive Research, A Division of Pacific-Sierra Research Corporation, 2901 28th Street, Santa Monica, California 90405-2938.

Jensen, K.F., 2001. Microreaction engineering—Is small better? Chem. Eng. Sci. 56, 293–303.

Jones, S.W., Thomas, O.M., Aref, H., 1989. Chaotic advection by laminar flow in a twisted pipe. J. Fluid Mech. 209, 335–357.

Kim, M., Yi, M., Zhong, J., Bau, H.H., Hu, H., Ananthasuresh, G.K. 1998. The fabrication of flow conduits in ceramic tapes and the measurement of fluid flow through these conduits. Micro-Electro-Mechanical Systems (MEMS). DSC vol. 66. pp. 171–177.

Liu, R.H., Stremler, M.A., Sharp, K.V., Olsen, M.G., Santiago, J.G., Adrian, R.J., Aref, H., Beebe, D.J., 2000. Passive mixing in a three-dimensional serpentine micro-channel. J. Micro-Electromech. Syst. 9, 190–197.

Mokrani, A., Castelain, C., Peerhossaini, H., 1997. The effect of chaotic advection on heat transfer. Int. J. Heat Mass Transfer 40, 3089–3104.

Qian, S., Bau, H.H., 2002. A chaotic electroosmotic stirrer. Anal. Chem. 74 (15), 3616–3625.

Qian, S., Zhu, J., Bau, H.H., 2002. A stirrer for magneto-hydrodynamically controlled micro fluidic networks. Phys. Fluids 14 (10), 3584–3592.

Sawyers, D., Sen, M., Chang, H., 1996. Effect of chaotic interfacial stretching on bimolecular chemical reaction in helical-coil reactors. Chem. Eng. J 64, 129–139.

Stremler, M.A., Olsen, M.G., Adrian, R.J., Aref, H., Beebe, D.J., 2000. Chaotic mixing in microfluidic systems, solid-state sensor and actuator workshop, Hilton Head, SC, June 4–8.

Yi, M., 2001. PhD Thesis, University of Pennsylvania.

Yi, M., Bau, H.H., 2000. The kinematics of bend-induced stirring in micro-conduits. In: IMECE 2000, MEMS 2000 Symposium Proceedings, pp. 489–496.

Yi, M., Qian, S., Bau, H.H., 2002. A magneto-hydrodynamic (MHD) chaotic Stirrer. J. Fluid Mech. 468, 153–177.